Journal of Nuclear Medicine, published on June 16, 2010 as doi:10.2967/jnumed.109.071753

Evaluation of ^{11}C-GSK189254 as a Novel Radioligand for the H_3 Receptor in Humans Using PET

Sharon Ashworth[1], Eugenii A. Rabiner[1], Roger N. Gunn[1], Christophe Plisson[1], Alan A. Wilson[2], Robert A. Comley[1], Robert Y.K. Lai[3], Antony D. Gee[1], Marc Laruelle[3], and Vincent J. Cunningham[1,4]

[1]GlaxoSmithKline Clinical Imaging Centre and Imperial College London, London, United Kingdom; [2]The Centre for Addiction and Mental Health (CAMH), Toronto, Ontario, Canada; [3]Neurosciences CEDD, GlaxoSmithKline, Harlow, United Kingdom; and [4]Aberdeen Biomedical Imaging Centre, School of Medical Sciences, University of Aberdeen, Aberdeen, United Kingdom

The histamine H_3 receptor is implicated in the pathophysiology of several central nervous system disorders. *N*-methyl-6-(3-cyclobutyl-2,3,4,5-tetrahydro-1*H*-benzo[*d*]azepin-7-yloxy)-nicotamide (GSK189254) is a highly potent, selective, and brain-penetrant H_3 receptor antagonist. Previous studies in the pig using PET have shown that ^{11}C-GSK189254 uptake in H_3-rich regions of the brain can be blocked by the selective H_3 antagonist ciproxifan. The purpose of the present study was to evaluate ^{11}C-GSK189254 as a PET radioligand for human studies and to determine the dose–receptor occupancy relationship of GSK189254 in the human brain. **Methods:** Dynamic PET scans were obtained in healthy subjects over 90 min after intravenous administration of approximately 370 MBq of ^{11}C-GSK189254. Blood samples were taken throughout the scans to derive the arterial plasma parent input function. Each subject was scanned twice, either with tracer alone (test–retest) or before and after a single oral dose of GSK189254 (10–100 μg). Data were analyzed by compartmental analysis, and regional receptor-occupancy estimates were obtained by graphical analysis of changes in the total volumes of distribution (V_T) of the radioligand. **Results:** ^{11}C-GSK189254 readily entered the brain; its regional brain distribution reflected the known distribution of H_3 receptors, with high binding in the caudate and putamen, intermediate binding in cortical regions, and low binding in the cerebellum. GSK189254 displayed a high receptor affinity, and a marked reduction in V_T was apparent at all the doses tested. The oral dose equaling 50% occupancy of the available receptor sites (ED_{50}) was estimated as 4.33 μg. Additional data on plasma pharmacokinetics after oral dosing and the plasma free fraction gave a corresponding estimate of the free concentration of GSK189254 required to occupy 50% of the available receptor sites (EC_{50}) (0.011 nM). The test–retest data showed reductions in regional V_T on the second scan in all subjects. A nonlinear compartmental analysis of this effect demonstrated that this reduction was consistent with carryover of a tracer mass dose effect with an estimated in vivo apparent dissociation constant of 0.010 nM, close to the independent estimate of the plasma EC_{50}. **Conclusion:** ^{11}C-GSK189254 can be used to quantify H_3 receptor availability in humans in vivo using PET but requires high specific activity; the possibility of tracer mass dose effects should be carefully analyzed.

Key Words: neurology; PET; radiopharmaceuticals; brain; GSK189254; H_3 receptor; human

J Nucl Med 2010; 51:1021–1029
DOI: 10.2967/jnumed.109.071753

Central histaminergic neurones originate almost exclusively in the tuberomammillary nucleus of the posterior hypothalamus and project to almost all regions of the mammalian brain (*1*). Histamine has a global coordinating function in the brain (*2*), particularly in relation to the regulation of the sleep–wake cycle (*3*), and mediates its biologic effects through activation of 4 transmembrane G-protein–coupled receptors (H_1, H_2, H_3, and H_4) (*4,5*). H_3 receptors are heterogeneously expressed in the mammalian brain, with particularly high densities in the basal ganglia (*6*). They are located presynaptically on histaminergic neurones, where they act as autoreceptors regulating the synthesis and release of histamine (*7*). In addition, H_3 receptors act as heteroreceptors on nonhistaminergic neurones, controlling the release of other neurotransmitters, including acetylcholine and dopamine (*8,9*).

The H_3 receptor has been implicated in a range of disorders including cognitive deficits, obesity, diabetes mellitus, and sleep disorders (*3,10,11*). Considerable interest in the pharmacology of this receptor exists, and several pharmaceutical companies are actively researching and developing H_3 agonists and antagonists as drug candidates for the treatment of cognitive disorders (*12*).

Since the discovery of the H_3 receptor more than 25 y ago, several ligands, radiolabeled with either ^{3}H or ^{125}I, have been developed as probes for investigation of its physiology, pharmacology, and distribution within the brain, including ^{3}H-(*R*)α-methylhistamine and ^{125}I-iodoproxyfan

Received Oct. 20, 2009; revision accepted Jan. 12, 2010.
For correspondence or reprints contact: Sharon Ashworth, GlaxoSmithKline Clinical Imaging Centre, Imperial College London, Hammersmith Hospital, Du Cane Rd., London, W12 0NN, U.K.
E-mail: Sharon.Ashworth-1@gsk.com

(*13–15*). Until recently, there has been a lack of suitable radioligands for imaging of the H_3 receptor in vivo in the central nervous system of humans using PET. A few compounds previously investigated as potential radioligands for PET include the iodoproxyfan analog ^{18}F-fluoroproxyfan (*16*) and the thioperamide analog ^{18}F-VUF5000 (*17*). Although ^{18}F-fluoroproxyfan may still prove to be potentially useful to the imaging of H_3 receptors in the human brain, other compounds, including ^{18}F-VUF5000, do not show the appropriate characteristics necessary for successful imaging agents. ^{18}F-VUF5000, for instance, shows a lack of brain penetration.

Hamill et al. (*18*) have described 2 new H_3 inverse agonist PET radioligands that look promising for imaging and quantifying H_3 receptors. In addition, Plisson et al. (*19*) have described the radiosynthesis and preclinical evaluation of ^{11}C-*N*-methyl-6-(3-cyclobutyl-2,3,4,5-tetrahydro-1*H*-benzo[*d*]azepin-7-yloxy)-nicotamide (^{11}C-GSK189254) as a novel PET radioligand for the H_3 receptor. GSK189254 is a novel, highly potent, selective, and brain-penetrant H_3 receptor antagonist, with high affinity for both human and rat H_3 receptors (−log(10) Ki, where Ki is the inhibition constant, 9.59–9.90 and 8.51–9.17, respectively) (*20*). Previous studies in the pig have shown that ^{11}C-GSK189254 is brain-penetrant, has suitable kinetics for quantification, and demonstrates uptake (which can be blocked by the H_3 antagonist ciproxifan) in H_3-rich regions of the brain.

Here we describe the evaluation of ^{11}C-GSK189254 in the human brain using PET. Healthy volunteers underwent 2 scans, either under test–retest conditions or before and after an oral dose of GSK189254 (10–100 μg), to assess specific binding of ^{11}C-GSK189254 and determine the dose–H_3 receptor occupancy relationship of GSK189254 in the human brain.

MATERIALS AND METHODS

The study was performed at the Centre for Addiction and Mental Health, Toronto, on behalf of GlaxoSmithKline.

Radiochemistry

6-[(3-cyclobutyl-2,3,4,5-tetrahydro-1*H*-3-benzo[*d*]azepin-7-yl)oxy]-3-nicotamide (GSK185071B) and GSK189254 were synthesized at GlaxoSmithKline. ^{11}C-GSK189254 was prepared by ^{11}C-methylation of the carboxamide precursor GSK185071B with ^{11}C-iodomethane (*21*) inside a high-performance liquid chromatography (HPLC) sample loop using the previously described loop method (*22*). Briefly, the normethyl precursor (0.5 mg) was dissolved in a mixture of dimethylformamide (80 μL) and aqueous potassium hydroxide (2N, 2 μL) and reacted on the loop with trapped ^{11}C-iodomethane for 4 min at room temperature. After purification by HPLC (250 × 10 mm; 20/80 acetonitrile/0.1N ammonium formate, pH 4; 7 mL/min) (Luna C18; Phenomenex) and formulation in buffered saline, ^{11}C-GSK189254 was obtained with 15%−20% radiochemical yield (uncorrected for decay, from ^{11}C-CO_2) at 27 min after the end of bombardment.

Study Subjects

Data from 21 healthy volunteers (16 men and 5 women) with a mean age of 43 y (range, 35–67 y) are reported for this study. Each subject underwent a physical examination, including a 12-lead electrocardiogram, vital-sign assessment, and blood analyses for substances of abuse. Each subject provided written informed consent, and the study was approved by the local research ethics board and Health Canada. On each day of PET, the subjects were cannulated in the forearm or antecubital vein for tracer administration and in the contralateral radial artery for blood sampling.

PET with ^{11}C-GSK189254

Each subject was scanned twice on a Biograph HiRez XVI PET camera system (Siemens Molecular Imaging), the performance characteristics of which are described by Brambilla et al. (*23*). On each scanning occasion, a scout view was acquired for the accurate positioning of the subject, followed by a low-dose (effective dose, 0.2 mSv) CT scan. A 511-keV attenuation image was generated from this CT image, which was then forward-projected to generate the attenuation correction for the emission PET sinograms. After the transmission scan, a 32-bit, list-mode 90-min emission scan was acquired. ^{11}C-GSK189254 (247–433 MBq) was administered by intravenous bolus injection via a cannula. The specific activity at the time of injection was 18.0–79.5 GBq/μmol. Because GSK189254 has a molecular weight of 351.5, the mass dose associated with these injections was 1.63–4.82 μg. The emission list-mode data were rebinned into a series of 3-dimensional sinograms (span, 11; ring difference, 27). Frames were defined as 1 × background frame (start of scan to time of injection, ~1 min), 8 × 15 s, 3 × 60 s, 5 × 120 s, 5 × 300 s, and 5 × 600 s. For each 3-dimensional sinogram, the data were normalized, and attenuation and scatter were corrected before Fourier rebinning was applied to convert the 3-dimensional sinograms into 2-dimensional sinograms. The 2-dimensional sinograms were then reconstructed into image space using a 2-dimensional filtered backprojection algorithm, with a ramp filter at a Nyquist cutoff frequency. After reconstruction, a gaussian filter (5 mm full width at half maximum) and calibration factor were applied.

Six of the subjects underwent 2 baseline scans (test–retest), with approximately 2 h between scan starts. Fifteen subjects received 1 baseline scan and an oral dose of GSK189254 (10–100 μg) at either 4 or 24 h before a second PET scan. Subjects also underwent 3-dimensional volumetric MRI using a fast spoiled gradient-recalled echo sequence acquired in the axial plane, to provide an anatomic image for coregistration with their PET data. MRI scans were obtained using a Signa Excite HD 1.5-T scanner system (GE Healthcare).

Blood Sampling and Metabolite Analysis

Arterial blood samples were collected continuously at a rate of 5 mL/min during the first 10 min after ^{11}C-GSK189254 administration. Further discrete samples were collected throughout each PET scan for measurement of the whole-blood radioactivity, plasma radioactivity, and parent fraction. For radiolabeled metabolite analyses, HPLC was performed by minor modifications of the method described by Hilton et al. (*24*). Briefly, plasma samples (4, 7, 10, 15, 30, 45, 60, and 75 min after ^{11}C-GSK189254 administration) were loaded onto a 5-mL HPLC injector loop (Valco) and injected onto a small capture column (4.6 × 20 mm) packed in-house with OASIS HLB (30 μm; Waters Corp.). The capture column was eluted with 1% aqueous acetonitrile (2 mL/min) for 3–4 min and then backflushed (25% acetonitrile/75% H_2O + 0.1N ammonium formate, pH 4, 2 mL/min) onto a 10-μm Luna C18 column (250 × 4.6 mm; Phenomenex). Both column effluents were monitored through a flow

jnm071753-pm ■ 6/10/10

detector (Flow-Count; Bioscan) operated in coincidence mode. All radioactivity data were corrected for physical decay and integrated using a personal computer. The recovery of radioactivity in the HPLC system was greater than 97% in all cases.

Kinetic Analysis of PET Data

A metabolite-corrected plasma input function was generated from the blood and plasma time–activity profiles and metabolite data. For each subject, regions of interest (ROIs) (cerebellum, insula cortex, anterior cingulate cortex, frontal cortex, parietal cortex, occipital cortex, caudate, putamen, hippocampus, amygdala, and thalamus) were defined on the MR image for that subject using a region template (*25*). The MR image was coregistered to each PET image for that subject using SPM2 (*26*). The ROIs were subsequently applied to the dynamic PET data to generate tissue time–activity curves. For presentation purposes, tissue radioactivity concentrations were normalized for the radioactive dose injected and for the subject's body mass, giving standardized uptake values ([kBq/mL of tissue]/[kBq/g of body mass]). Data are presented as mean ± SD.

A 2-tissue-compartment model was applied to the plasma and tissue data, with rate constants K_1 and k_2 describing the exchange of tracer between plasma and tissue and rate constants k_3 and k_4 describing the exchange of tracer between the 2 tissue compartments. High initial estimates of K_1 indicated that there were significant dispersion effects in the measured blood activity, attributable to the length of the sampling cannula (~1.25 m). Delay and dispersion terms were therefore incorporated in the model (Appendix). Because of the slow kinetics and correspondingly high estimates of the total volumes of distribution (V_T) for this radioligand, it was also necessary to apply constraints to the model using a shared-parameter approach. Thus, individual estimates of K_1 and k_3 were obtained for each ROI, whereas estimates of the K_1/k_2 ratio and k_4 were obtained globally across all ROIs for each scan (Appendix). Time stability was analyzed by sequentially examining datasets with decreasing scan durations, allowing for an assessment of what scanning duration was required to obtain a stable estimate of the V_T in each region. Results are expressed in terms of the V_T (the equilibrium partition coefficient between tissue and plasma, $V_T = K_1/k_2(1 + k_3/k_4)$) for each ROI (*27*).

Because there was no suitable reference region within the brain to quantify free plus nonspecific binding (V_{ND}) (*27*), estimates of fractional occupancy (Occ) and V_{ND} for each subject were obtained by graphical analysis according to the occupancy plot described by Equation 1.

$$V_T^{Base} - V_T^{Drug} = Occ(V_T^{Base} - V_{ND}), \qquad \text{Eq. 1}$$

where V_T^{Base} and V_T^{Drug} are the V_Ts across all regions obtained at baseline and after drug administration, respectively (*28*).

Estimates of the oral dose of GSK189254 required for 50% occupancy of the available receptor sites (ED_{50}) were obtained by fitting an E_{max} model (Eq. 2) to a plot of fractional occupancy versus oral dose (D) across all subjects.

$$Occ = (E_{max} \times D)/(ED_{50} + D), \qquad \text{Eq. 2}$$

where E_{max} is the apparent maximal attainable occupancy.

Data were also available from a previous pharmacokinetic study of the concentration of the cold drug in plasma after oral administration, together with an estimate of the free fraction of the drug in plasma. These data were used to convert the ED_{50} to the equivalent free concentration of GSK189254 required to occupy 50% of the available receptor sites (EC_{50}), assuming passive transport of GSK189254 across the blood–brain barrier.

After the estimation of the EC_{50}, the test–retest data were analyzed further to investigate the possibility of the mass dose associated with the tracer injection affecting occupancy measurements. In brief, regional data from corresponding test and retest scans were fitted in sequence to a parallel 2-tissue-compartment model, with equations describing the time courses of radioactivity in nondisplaceable and specifically bound compartments together with the concentration time courses of cold drug in the 2 compartments (Appendix).

RESULTS

Representative images from the baseline scans are shown in Figure 1. After intravenous administration of ^{11}C-GSK189254, radioactivity readily entered the brain, accumulating in each ROI including the cerebellum. The distribution was heterogeneous, with highest concentrations in the caudate and putamen. Representative time–activity curves from a baseline scan are shown in Figure 2, together with a corresponding plasma parent input function. The parent fraction of ^{11}C-GSK189254 in plasma was 86% ± 5% after 75 min. The kinetics of the uptake of ^{11}C-GSK189254 in the brain were slow in that there was no obvious washout phase in the regional time–activity curves within the time frame of the baseline scans. Attempts to fit compartmental models to high-binding individual regions alone frequently gave unrealistic estimates of V_T because of large errors in the off-rate constant (k_4). Fits were therefore obtained by simultaneous analysis of all regions, applying the constraints described in the "Materials and Methods" section, with global estimates of the K_1/k_2 ratio, k_4, and dispersion rate constant (k_{disp}) for each scan.

[Fig. 1] [Fig. 2]

Test–retest results are shown in Table 1. In each region studied, there was a significant reduction in V_T in the second scan relative to the first. The significance of this observation will be commented on later.

[Table 1]

Figures 1 and 2 show the reduction in the overall brain uptake of ^{11}C-GSK189254 after oral administration of GSK189254. A marked reduction in V_T was apparent at all the doses tested, even doses as low as 10 μg (Table 2). This effect was seen in all regions, including the cerebellum, which was therefore unsuitable for use as a reference region devoid of specific binding.

[Table 2]

The overall estimate of k_{disp} was 0.025 ± 0.016 s^{-1}. Simulations (results not shown) demonstrated a negligible propagation of error from k_{disp} to V_T.

The effects of scan length on the stability of estimates of V_T are illustrated in Figure 3. There was no apparent bias in low-, intermediate-, or high-binding regions, but as expected for this slow ligand the increase in variance was more marked in high-binding regions, indicating a need for maximal scanning times.

[Fig. 3]

jnm071753-pm ■ 6/10/10

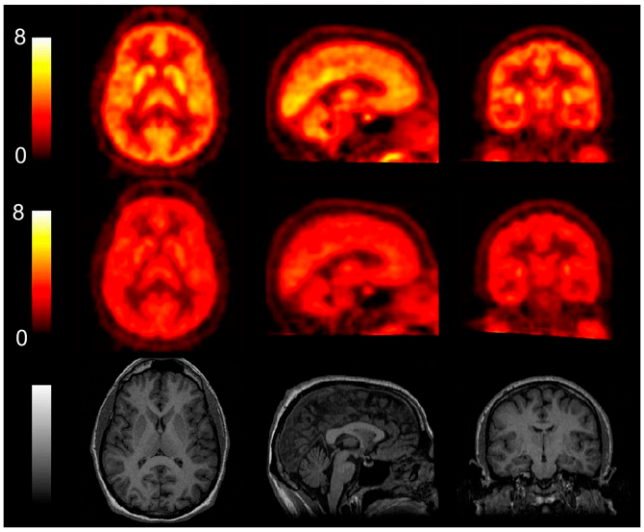

RGB

FIGURE 1. Representative PET images after ^{11}C-GSK189254 administration to a healthy human subject before (top) and 4 h after (middle) a 50-μg oral dose of GSK189254. Mean standardized uptake value images over 0–90 min are shown with structural MR image for same subject (bottom).

The estimate of the K_1/k_2 ratio for the scans reported in Table 2 was 4.4 ± 3.4. However, because this estimate is not a stable macroparameter (*29*) in the absence of a suitable reference region, estimates of receptor occupancy and V_{ND} were therefore obtained from occupancy plots as described in the "Materials and Methods" section.

[**Fig. 4**] Figure 4 shows occupancy plots for each subject who received GSK189254 at 4 h before the second scan. Occupancies were high across all doses including the lowest oral dose of 10 μg. High occupancies were also seen 24 h after an oral dose of 25 μg (67.6 ± 12.2, n = 5), consistent with the persistence of the drug in the systemic circulation. The overall estimate of V_{ND} was 10.54 ± 1.78.

[**Fig. 5**] The relationship between dosage and receptor occupancy at 4 h for GSK189254 is shown in Figure 5. A least-squares fit of Equation 2 to these data gave an estimate of ED_{50} = 0.055 ± 0.014 μg/kg of body weight. The mean body weight of these subjects was 79.4 kg, corresponding to an oral dose ED_{50} of 4.33 μg per subject. In-house data were available on the plasma concentration time course of GSK189254 in human volunteers after a range of oral doses from 25 to 500 μg per subject. These data were normalized to the ED_{50}, assuming linearity, giving a mean plasma concentration over the scanning period (4–5.5 h) of 0.031 nM. A 0.36 value for the plasma free fraction (f_P) (in-house data) gives an EC_{50} of 0.011 nM.

This observation of high occupancies at low oral doses suggested that a decrease in V_T in retest data relative to test data could be due to a tracer mass dose effect with carryover from the test to the retest scan, even at the low mass doses (<5 μg) associated with the injection of ^{11}C-GSK189254. The test–retest data were therefore reanalyzed using a model taking account of this carryover, formulated in terms of a regional binding capacity (B_{max}) and apparent dissociation constant (K_D) with occupancy of receptor sites varying over time (Appendix). Although the test–retest part of the study was clearly not originally designed as a saturation experiment, it was nonetheless possible in this way to obtain an independent estimate of the K_D by simultaneously fitting multiple regions across the test and retest scans. Satisfactory fits were obtained in 5 of 6

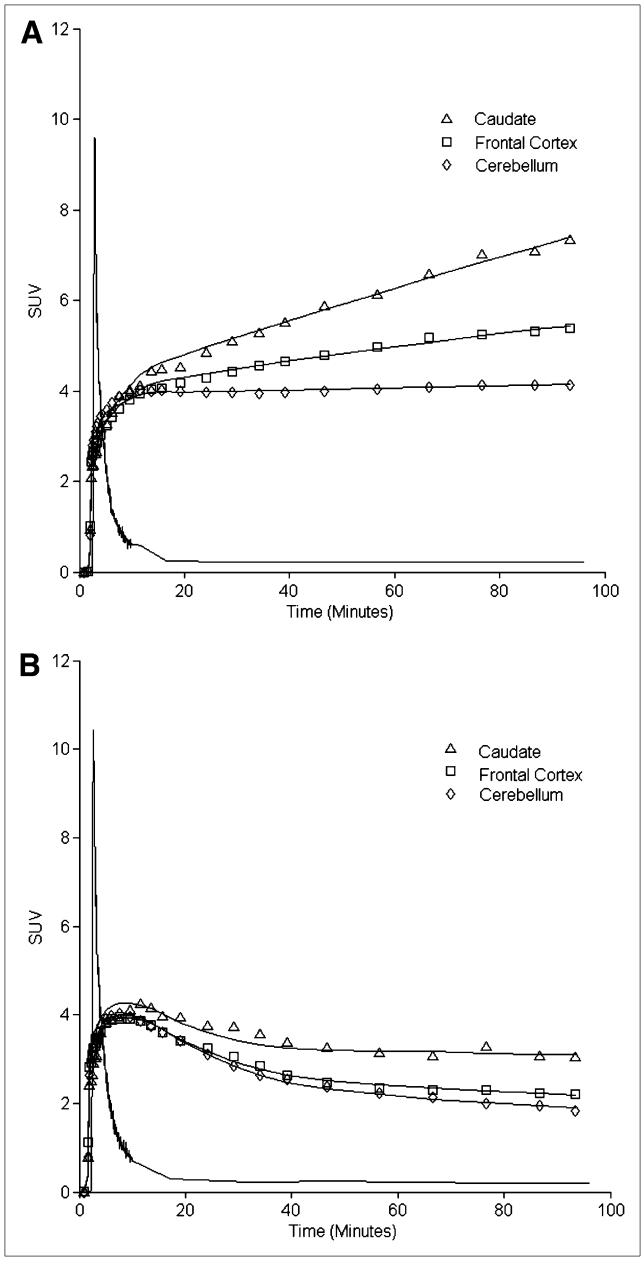

FIGURE 2. Typical time–activity curves from 1 subject and corresponding plasma input functions after intravenous administration of ^{11}C-GSK189254 at baseline (A) and 4 h after 100 μg of GSK189254 (B), together with corresponding best fits. SUV = standardized uptake value.

jnm071753-pm ■ 6/10/10

TABLE 1. Estimates of V_T for Brain ROIs from Test–Retest Scans

ROI	Test (mean ± SD)	Retest (mean ± SD)
Caudate	96.7 ± 31.2	61.9 ± 27.6
Putamen	119 ± 21.7	68.4 ± 8.9*
Cerebellum	22.5 ± 4.5	17.6 ± 2.7*
Frontal cortex	32.0 ± 3.4	23.3 ± 1.9†
Parietal cortex	26.8 ± 3.1	20.5 ± 1.6†
Occipital cortex	23.9 ± 3.6	18.5 ± 2.0*
Insular cortex	47.4 ± 12.4	30.4 ± 2.6‡
Anterior cingulate cortex	50.2 ± 13.3	50.2 ± 13.3‡
Hippocampus	26.3 ± 4.0	20.7 ± 4.6†
Amygdala	42.3 ± 3.4	30.0 ± 5.3*
Thalamus	24.5 ± 1.8	19.8 ± 2.1*

*$P < 0.005$.
†$P < 0.0005$.
‡$P < 0.05$.
Statistical comparisons were performed using 2-tailed Student *t* test.

[**Fig. 6**] [**Table 3**]

subjects, with 1 outlier. A typical fit is shown in Figure 6, and the results are summarized in Table 3.

The estimation of K_D in Table 3 (0.0095 nM) used the mean value of V_{ND} (10.54) and f_P (0.36) (Appendix). This estimate of K_D agrees well with that of the plasma EC_{50} obtained from the analysis of the occupancy studies (0.011 nM). This agreement is consistent with the possibility that the reduction in V_T between test and retest (Table 2) was due to a tracer mass dose effect. Estimates of B_{max} for low (cerebellum), high (putamen), and intermediate (cortex) regions are also shown in Table 3.

DISCUSSION

The present study was designed to investigate ^{11}C-GSK189254 in the human brain and to determine the dose–H_3 receptor occupancy relationship of GSK189254. All scans were performed during normal waking hours when the levels of histamine in the brain are known to be stable (*30*).

After intravenous administration of ^{11}C-GSK189254 in humans, the regional distribution of radioactivity in the brain was consistent with the known distribution of H_3 receptors (*6*). Two key issues had to be addressed in the analysis. The first was the slow off-rate of the radioligand from the receptor. The constraints that were applied to the 2-tissue-compartment model relating tissue and plasma data assume that regional differences in ^{11}C-GSK189254 kinetics are due to differences in delivery and available receptor density but that nondisplaceable binding and receptor off-rates are the same across regions. The resultant baseline estimates of V_T were high in all regions, particularly in the putamen (98 ± 50) and caudate (74 ± 27). The stability of these estimates was investigated by successive removal of late–time frame data from the analyses. No apparent bias in low-, intermediate-, or high-binding regions was observed, indicating the suitability of the modeling approach.

The second issue was the lack of a suitable reference region devoid of specific binding. Estimates of V_{ND}, required for the calculation of occupancy after oral dosing, were therefore derived from occupancy plots. Linear plots, indicating occupancy to be the same across all ROIs after oral dosing of GSK189254, were obtained for all subjects, with consistent estimates of V_{ND} being obtained from the intercepts.

Given the estimate of V_{ND}, together with a value for the f_P (from which the tissue free fraction could be obtained), it was then possible to obtain 2 essentially independent estimates of the in vivo affinity of GSK189254 for its receptor sites, assuming passive diffusion. The first, using a conventional estimate of the oral ED_{50}, together with plasma pharmacokinetic data, gave an in vivo plasma EC_{50} of 0.011 nM. The second, from an analysis of a carryover effect in the test–retest data, together with the known tracer

TABLE 2. Estimates of Regional V_T Before and After Oral Administration of GSK189254

ROI	Baseline (n = 15)	4 h after administration of... 100 μg (n = 1)	50 μg (n = 3)	25 μg (n = 2)	10 μg (n = 3)	24 h after administration of 25 μg (n = 6)
Caudate	69.9 ± 26.9*	15.0	15.8 ± 3.2	16.1	24.8 ± 4.2	30.7 ± 18.7*
Putamen	95.2 ± 7.8	17.3	22.2*	25.7	31.5 ± 5.3	44.6 ± 18.5
Cerebellum	22.2 ± 3.5	8.50	10.5 ± 0.8	10.5	14.2 ± 1.8	14.5 ± 2.5
Frontal cortex	28.4 ± 4.2	9.95	12.3 ± 0.9	12.1	16.2 ± 2.9	17.9 ± 3.5
Parietal cortex	24.2 ± 3.7	9.53	11.6 ± 0.5	10.8	14.6 ± 2.3	16.3 ± 3.2
Occipital cortex	21.8 ± 3.2	9.12	11.4 ± 0.8	10.5	13.5 ± 1.7	15.4 ± 2.2
Insula cortex	38.7 ± 7.1	12.6	14.8 ± 1.4	16	19.2 ± 3.1	23.5 ± 4.0
Anterior cingulate cortex	44.8 ± 14.6	12.6	14.5 ± 1.4	16.4	21.0 ± 4.0	23.3 ± 4.6
Hippocampus	22.8 ± 3.6	9.25	10.1 ± 0.8	10	13.4 ± 1.5	15.0 ± 2.7
Amygdala	36.5 ± 10.6	10.9	12.1 ± 0.5	14.9	17.5 ± 3.9	20.6 ± 5.3
Thalamus	23.5 ± 3.4	10.7	11.2 ± 0.9	10.7	15.0 ± 2.2	16.5 ± 3.7

*Caudate or putamen could not be fitted for 1 subject.

jnm071753-pm ■ 6/10/10

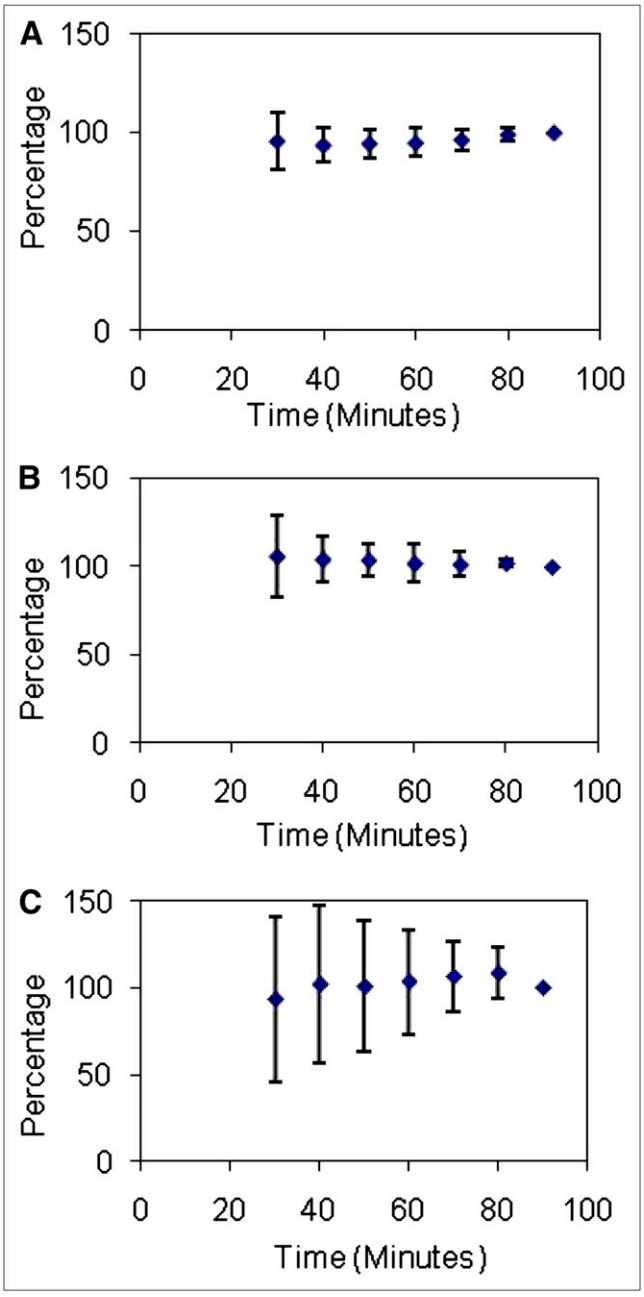

RGB

FIGURE 3. Assessment of stability of V_T estimates from differing baseline scan durations for cerebellum (A), frontal cortex (B), and putamen (C). Data are presented as mean percentage (±SD) of value obtained using full 90-min dataset.

specific activities, gave a tissue K_D of 0.0095 nM. If there was also carryover in the postdose scans, simulations (not shown) indicated that this carryover would be negligible at high occupancies and that the occupancies quoted in this study would be slightly underestimated.

The affinities measured in vivo using PET, equivalent to a negative log of the dissociation constant (*pK*) of about 11, is an order of magnitude higher than that measured in vitro for the human H_3 receptor (pK = 9.59–9.90) (*20*). In contrast, in a previous study in the pig, the estimate of the in vivo *pK* using PET (9.9) was similar to the in vitro estimate, both being an order of magnitude lower than that seen here in humans, with the tracer kinetics being more obviously reversible in vivo (*19*). The estimated receptor densities are, however, similar in the 2 species. The reason for this interspecies difference does not appear to be that GSK189254 is a P-glycoprotein substrate in the pig, because brain uptake of this compound in vivo at tracer doses was not affected by cyclosporine A (C. Salinas, unpublished data, 2009). Differences in the concentration of endogenous histamine are unlikely to contribute to the observed interspecies difference, and we therefore do not have an explanation for this difference in the affinity of GSK189254.

CONCLUSION

In general, care must be taken when using high-affinity PET radioligands to maintain a negligible level of receptor occupancy by the radioligand itself during the scan acquisition. Typically for an ideal PET radioligand, the mass dose associated with its injection should not occupy more than about 5% of the available receptors. This mass dose limitation needs to be considered in future study designs if ^{11}C-GSK189254 is to be used to measure H_3 receptor occupancy of other compounds in humans. Suitable time intervals between PET acquisitions will be required to allow for the washout of the mass dose associated with baseline scans before postdose scans. The ED_{50} estimated here would correspond to a dose of no more than 0.003 μg/kg of body weight to achieve less than 5% occupancy. Alternatively, a higher tracer mass dose effect could be accounted for by modeling as shown here, particularly if relative biases between baseline and posttreatment scans are minimized by the administration of similar tracer mass doses in the 2 scans.

APPENDIX

A 2-Tissue-Compartment Model Incorporating Dispersion of Input Function

Preliminary investigation of the data showed that a reversible 2-tissue-compartment (4k) model was necessary to fit low-binding regions but gave unreasonable estimates of K_1, indicating a dispersion effect. The operational equation of a catenary 2-tissue-compartment model with a true arterial plasma input function ($C_A(t)$) is given by (*29*):

$$C_T(t) = K_1 C_A(t) \otimes (\Phi_1 e^{-\theta_1 t} + \Phi_2 e^{-\theta_2 t}), \qquad \text{Eq. 1A}$$

where t is time; $C_T(t)$ the total tissue activity; K_1 the plasma-to-tissue clearance; and Φ_1, Φ_2, θ_1, and θ_2 are functions of the rate constants k_2, k_3, and k_4, describing the exchange of tracer between plasma and tissue compartments (*27*). ⊗ denotes convolution.

Assuming a simple exponential dispersion function (*31*), then the measured input function ($C_M(t)$) is given by:

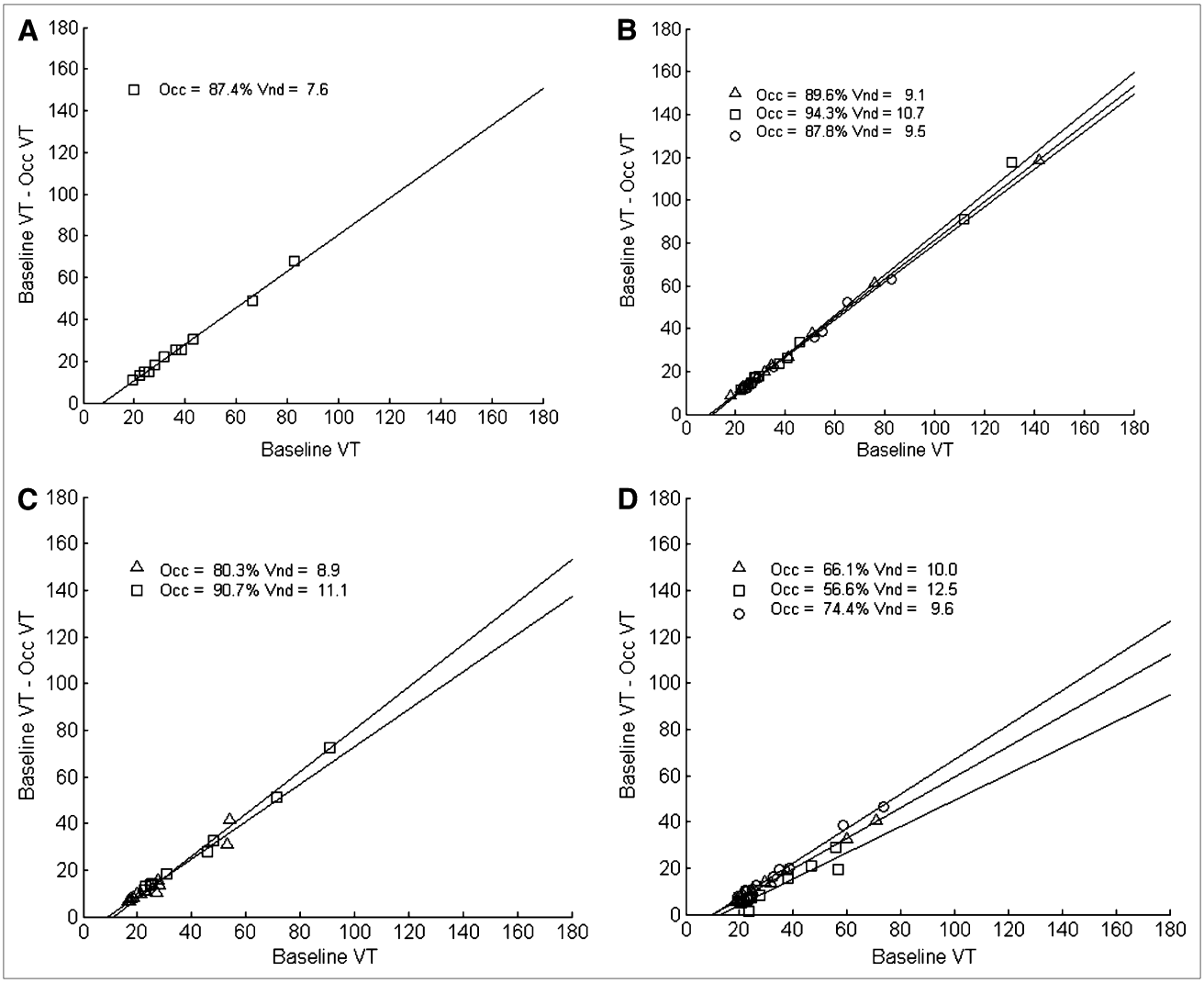

FIGURE 4. Graphical estimation of occupancy and V_{ND} of GSK189254. Occupancy is given by slope and V_{ND} by intercept with *x*-axis. Each data point represents difference in V_T for single ROI for individual subjects before and 4 h after GSK189254 administration at 100-μg (n = 1) (A), 50-μg (n = 3) (B), 25-μg (n = 2) (C), and 10-μg (n = 3) (D) doses.

$$C_M(t) = k_{disp} C_A(t) \otimes e^{-k_{disp} t}. \qquad \text{Eq. 2A}$$

Substitution of $C_A(t)$ by $C_M(t)$ in Equation 1A then gives:

$$C_T(t) = (K_1/k_{disp})(C_M(t) + C_M(t) \otimes (\Phi_3 e^{-\theta_1 t} + \Phi_4 e^{-\theta_2 t})), \qquad \text{Eq. 3A}$$

where Φ_3 and Φ_4 are functions of k_2, k_3, k_4, and k_{disp}. The particular formulation of these functions is equivalent to those of a full reference-tissue model treating $C_M(t)$ as the reference input (*29*), with V_{ND} equaling 1 and turnover rate constant equaling k_{disp}.

Sharing of Common Parameters Across Regions Within Scans

The above model involves 5 identifiable parameters, K_1, k_2, k_3, k_4, and k_{disp}. Estimating these parameters independently for each ROI gave acceptable fits and residuals (results not shown) but frequently with unreasonable numeric estimates of the individual parameters (e.g., negative values) or outlying large estimates of V_T for high-binding regions. Constraints were therefore applied by minimizing the residual sum of squares simultaneously across all regions, with individual estimates of K_1 and k_3 for each region but with common (global) estimates of K_1/k_2, k_4, and k_{disp}.

Estimation of Tracer Mass Dose Effect and of Carryover Between Test–Retest Scans

The aim of the modeling was to obtain estimates of K_D and B_{max} from test–retest data, using a simple competition model.

Parallel 2-tissue-compartment models were set up (*32*) describing the kinetics of ^{11}C-GSK189254 and of unlabeled GSK189254, coupling the test–retest scans and taking into

jnm071753-pm ■ 6/10/10

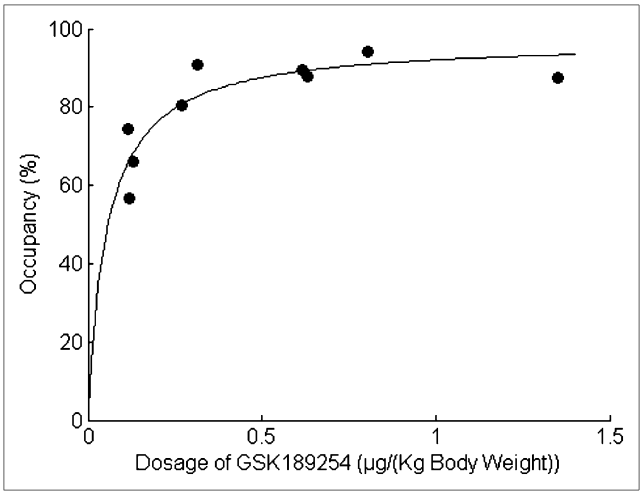

FIGURE 5. Dose–occupancy relationship of orally administered GSK189254 (4 h after dosing), together with least-squares fit of Equation 2 to data.

account the different specific activities of the injected doses and the carryover of mass dose from the first to the second scan. Carryover of radioactivity between scans was assumed to be negligible, because of decay, but the initial-condition concentrations of unlabeled GSK189254 in tissue compartments at the start of the retest scan were calculated by extrapolation of the fits to the test scan. This was achieved by applying a single exponential extrapolation to the tail of the input functions over the approximately 30-min period between the end of the first scan and the beginning of the second and calculating the corresponding compartmental concentrations as initial conditions for the second scan. The input functions were precorrected for dispersion with the mean estimate of k_{disp} obtained from fits to individual scans using Equation 3A.

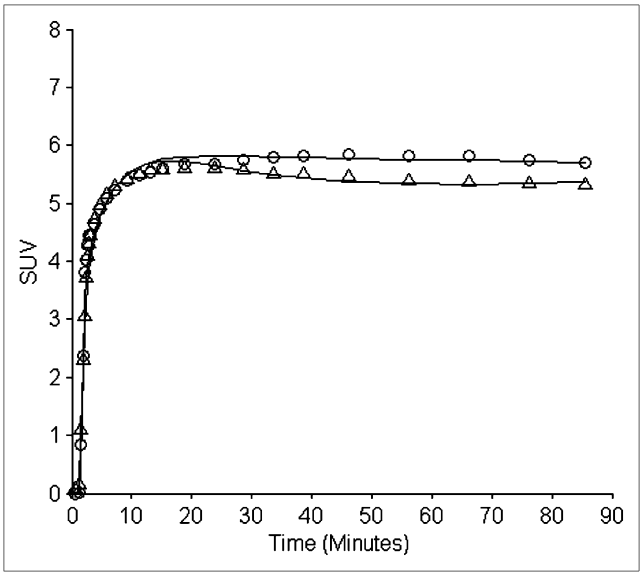

FIGURE 6. Typical fits to representative occipital time–activity curves from 1 subject after intravenous administration of ^{11}C-GSK189254. Standardized uptake values are shown from test (○) and retest (△) scans illustrating carryover effect. SUV = standardized uptake value.

TABLE 3. Estimates of B_{max} and K_D Obtained from Test–Retest Data

Subject no.	k_{off} (min^{-1})	K_D (nM)	B_{max} (nM)		
			Cerebellum	Occipital cortex	Putamen
1	0.015	0.0131	0.74	0.95	5.1
2	0.021	0.0093	0.75	0.69	4.1
3	0.031	0.0064	0.48	0.62	2.9
4	0.029	0.0094	0.66	0.75	3.6
5	0.020	0.0093	0.33	0.50	3.1
Mean	0.023	0.0095	0.59	0.70	3.8
SD	0.007	0.0024	0.18	0.17	0.9

k_3 varies in time throughout the 2 scans according to the following equation:

$$k_3(t) = f_{ND}\, k_{on}(B_{max} - D_S(t)), \qquad \text{Eq. 4A}$$

where $D_S(t)$ is the concentration of the unlabeled GSK189254 in the specifically bound compartment. B_{max}, f_{ND}, k_{on}, and k_4 ($=k_{off}$) are time-invariant.

The model was parameterized in terms of K_1, V_{ND}, k_{off}, K_D^{ND}, and B_{max}, where

$$K_D^{ND} = \frac{k_{off}}{k_{on} f_{ND}}. \qquad \text{Eq. 5A}$$

Equations were integrated numerically. V_{ND} was fixed (see main text), and the remaining parameters were estimated using a Levenberg–Marquardt algorithm. Under the assumption of passive diffusion, an estimate of f_{ND} was derived from the measured f_P:

$$f_{ND} = fp/V_{ND}. \qquad \text{Eq. 6A}$$

This then allows for the true K_D to be derived as

$$K_D = f_{ND} K_D^{ND}. \qquad \text{Eq. 7A}$$

Individual estimates of K_1 were obtained for each region and scan, and estimates of B_{max} were obtained for each region across test and retest scans. K_D and k_{off} were treated as common parameters (see above) within subjects across regions and across the 2 scans.

ACKNOWLEDGMENTS

We thank staff of CAMH who carried out the acquisition of the data and provided care for the subjects while they underwent the procedures.

REFERENCES

1. Watanabe T, Taguchi Y, Shiosaka S, et al. Distribution of the histaminergic neuron system in the central nervous system of rats: a fluorescent immunohistochemical analysis with histidine decarboxylase as a marker. *Brain Res.* 1984; 295:13–25.
2. Brown RE, Stevens DR, Haas HL. The physiology of brain histamine. *Prog Neurobiol.* 2001;63:637–672.
3. Parmentier R, Anaclet C, Guhennec E, et al. The brain H_3-receptor as a novel therapeutic target for vigilance and sleep-wake disorders. *Biochem Pharmacol.* 2007;73:1157–1171.
4. Hill SJ, Ganellin CR, Timmerman H, et al. International union of pharmacology. XIII. Classification of histamine receptors. *Pharmacol Rev.* 1997;49:253–278.
5. Nguyen T, Shapiro DA, George SR, et al. Discovery of a novel member of the histamine receptor family. *Mol Pharmacol.* 2001;59:427–433.
6. Martinez-Mir MI, Pollard H, Moreau J, Arrang JM, Ruat M, Traiffort E. Three histamine receptors (H_1, H_2 and H_3) visualised in the brain of human and non-human primates. *Brain Res.* 1990;526:322–327.
7. Arrang JM, Garbarg M, Schwartz JC. Auto-inhibition of brain histamine release mediated by a novel class (H_3) of histamine receptor. *Nature.* 1983;302:832–837.
8. Molina-Hernandez A, Nunez A, Arias-Montano JA. Histamine H_3-receptor activation inhibits dopamine synthesis in rat striatum. *Neuroreport.* 2000;11: 163–166.
9. Prast H, Tran MH, Fischer H, et al. Histaminergic neurons modulate acetylcholine release in the ventral striatum: role of H_3 histamine receptors. *Naunyn Schmiedebergs Arch Pharmacol.* 1999;360:558–564.
10. Hancock AA, Fox GB. Perspectives on cognitive domains, H_3 receptor ligands and neurological disease. *Expert Opin Investig Drugs.* 2004;13:1237–1248.
11. Yoshimoto R, Miyamoto Y, Shimamura K, et al. Therapeutic potential of histamine H_3 receptor agonist for the treatment of obesity and diabetes mellitus. *Proc Natl Acad Sci USA.* 2006;103:13866–13871.
12. Celanire S, Wijtmans M, Talaga P, Leurs R, de Esch IJP. Histamine H_3 receptor antagonists reach out for the clinic. *Drug Discov Today.* 2005;10:1613–1627.
13. Arrang JM, Garbarg M, Lancelo JC, et al. Highly potent and selective ligands for histamine H_3-receptors. *Nature.* 1987;327:117–123.
14. Ligneau X, Garbarg M, Vizuete ML, et al. [^{125}I]Iodoproxyfan, a new antagonist to label and visualize cerebral histamine H_3 receptors. *J Pharmacol Exp Ther.* 1994;271:452–459.
15. Krause M, Stark H, Schunack W. Iododestannylation: an improved synthesis of [^{125}I]iodoproxyfan, a specific radioligand of the histamine H_3 receptor. *J Labelled Comp Radiopharm.* 1997;39:601–606.
16. Iwata R, Horváth G, Pascali C, et al. Synthesis of 3-[^{1}H-imidazol-4-yl]propyl4-[^{18}F]fluorobenzyl ether ([^{18}F]fluoroproxyfan): a potential radioligand for imaging histamine H_3 receptors. *J Labelled Comp Radiopharm.* 2000;43:873–882.
17. Windhorst AD, Timmerman H, Klok RP, et al. Evaluation of [^{18}F]VUF 5000 as a potential PET ligand for brain imaging of the histamine H_3 receptor. *Bioorg Med Chem.* 1999;7:1761–1767.
18. Hamill TG, Sato N, Jitsuoka M, et al. Inverse agonist histamine H_3 receptor PET tracers labelled with carbon-11 or fluorine-18. *Synapse.* 2009;63:1122–1132.
19. Plisson C, Gunn RN, Cunningham VJ, et al. ^{11}C-GSK189254: a selective radioligand for *in vivo* central nervous system imaging of histamine H_3 receptors by PET. *J Nucl Med.* 2009;50:2064–2072.
20. Medhurst AD, Atkins AR, Beresford IJ, et al. GSK189254: a novel H_3 receptor antagonist that binds to histamine H_3 receptors in Alzheimer's disease brain and improves cognitive performance in preclinical models. *J Pharmacol Exp Ther.* 2007;321:1032–1045.
21. Wilson AA, DaSilva JN, Houle S. Facile radiolabelling and purification of 2*B*-[*O*-$^{11}CH_3$]-carbomethoxy-3*B*-aryltropanes: radiotracers for the dopamine transporter. *J Labelled Comp Radiopharm.* 1994;34:759–766.
22. Wilson AA, Garcia A, Jin L, Houle S. Radiotracer synthesis from [^{11}C]-iodomethane: a remarkably simple captive solvent method. *Nucl Med Biol.* 2000; 27:529–532.
23. Brambilla M, Secco C, Dominietto M, Matheoud R, Sacchetti G, Ingelese E. Performance characteristics obtained for a new 3-dimensional lutetium oxyorthosilicate-based whole-body PET/CT scanner with the National Electrical Manufacturers Association NU 2-2001 Standard. *J Nucl Med.* 2005;46:2083–2091.
24. Hilton J, Yokoi F, Dannals RF, Ravert HT, Szabo Z, Wong DF. Column-switching HPLC for the analysis of plasma in PET imaging studies. *Nucl Med Biol.* 2000;27:627–630.
25. Hammers A, Koepp MJ, Free S, et al. Implementation and application of a new brain template for multiple volumes of interest. *Hum Brain Mapp.* 2002;15:165–174.
26. Wellcome Trust Centre for Neuroimaging. Statistical Parametric Mapping. Available at: http://www.fil.ion.ucl.ac.uk/spm. Accessed May 6, 2010.
27. Innis RB, Cunningham VJ, Delforge J, et al. Consensus nomenclature for *in vivo* imaging of reversibly binding radioligands. *J Cereb Blood Flow Metab.* 2007;27: 1533-1539.
28. Cunningham VJ, Rabiner EA, Slifstein M, Laruelle M, Gunn RN. Measuring drug occupancy in the absence of a reference region: the Lassen plot re-visited. *J Cereb Blood Flow Metab.* 2010;30:46–50.
29. Gunn RN, Gunn SR, Cunningham VJ. Positron emission tomography compartmental models. *J Cereb Blood Flow Metab.* 2001;21:635–652.
30. Chu M, Huang ZL, Qu WM, Eguchi N, Yao MH, Urade Y. Extracellular histamine level in the frontal cortex is positively correlated with the amount of wakefulness in rats. *Neurosci Res.* 2004;49:417–420.
31. Meyer E. Simultaneous correction for tracer arrival, delay, and dispersion in CBF measurements by the $H_2{}^{15}0$ autoradiographic method and dynamic PET. *J Nucl Med.* 1989;30:1069–1078.
32. Delforge J, Bottlaender M, Loc'h C, et al. Quantitation of extrastriatal D_2 receptors using a very high-affinity ligand (FLB 457) and the multi-injection approach. *J Cereb Blood Flow Metab.* 1999;19:533–546.